Fuel 223 (2018) 164–178

Contents lists available at ScienceDirect

Fuel

journal homepage: www.elsevier.com/locate/fuel

Full Length Article

Entrained flow gasification. Part 3: Insight into the injector near-field by Large Eddy Simulation with detailed chemistry

Georg Eckel[a,*], Patrick Le Clercq[a], Trupti Kathrotia[a], Alexander Saenger[b], Sabine Fleck[b], Marco Mancini[c], Thomas Kolb[b], Manfred Aigner[a]

[a] German Aerospace Center (DLR), Institute of Combustion Technology, Pfaffenwaldring 38-40, 70569 Stuttgart, Germany
[b] Karlsruhe Institute of Technology (KIT), Institute for Technical Chemistry, Postfach 3640, 76021 Karlsruhe, Germany
[c] Clausthal University of Technology, Institute of Energy and Process Engineering and Fuel Technology, Agricolastr. 4, 38678 Clausthal-Zellerfeld, Germany

ARTICLE INFO

Keywords:
Turbulent reacting multi-phase flow
Entrained flow gasification
Fuel conversion
Numerical simulation
Flame stabilization

ABSTRACT

Entrained flow gasification is a promising process for the conversion of low-grade feedstock, e.g. highly viscous slurries and suspensions with a significant content of solid particles, to high quality fuels. A major scientific challenge is the prediction of the physical and chemical phenomena occurring in such high-temperature and high-pressure multiphase flow systems. In this context, this article is the sequel to "Entrained flow gasification. Part 1: Gasification of glycol in an atmospheric-pressure experimental rig " [1] and "Entrained flow gasification. Part 2: Mathematical modeling of the gasifier using RANS method " [2]. The same strategy as in the first two parts was followed. In order to reduce complexity, this study focused on a two-phase (gas and liquid) flow system with a model fuel (mono-ethylene glycol) under the simplified conditions provided by the atmospheric lab-scale gasifier REGA. Using the experimental data set provided in Part 1 of the coordinated papers for validation purposes, the main focus of this study was on the detailed understanding of the near injector region of the entrained flow gasifier REGA. The unsteady flow and the chemical conversion in the gasifier were investigated by means of Large Eddy Simulations with a detailed chemistry solver including 44 individual species and a direct calculation of 329 chemical reactions. The dispersed phase was solved by Lagrangian Particle Tracking. Downstream comparisons with experimental data showed a reasonable agreement concerning temperature and species profiles. The analysis of the injector near-field revealed that the high temperature reaction zone close to the injector could not be explained by a direct reaction of the fuel with the oxidizer. Instead, carbon monoxide and hydrogen mainly formed on the axis were transported upstream by the recirculation zone. The reaction of CO and H_2 with the oxygen stabilized the flame. The heat release from this reactions supported the vaporization and decomposition of fuel as well as the downstream gasification reactions.

1. Introduction

As stated in Fleck et al. [1], the design and scale-up of entrained flow gasifiers, such as the bioliq® process plant, was mainly supported by experience and less by detailed understanding of the physical and thermo-chemical sub-processes involved. The main reason why detailed modeling and simulation of the key physical and chemical sub-processes occurring in any type of gasifier is a growing area of research is that gasification is an energy intensive process, which requires precise and rigorous engineering and well tuned operation in order to yield a positive energetic and economic balance. Actually, Computational Fluid Dynamics (CFD) is now a well established method in many industrial sectors necessitating strong R&D activities. Market and regulators often push for performance improvements and environmental impact reduction, which promotes the use of such tools. The aeronautic industry (air-framers and engine OEMs), the automobile industry, or even the micro-processor industry, to mention only a few, all rely on CFD and complex modeling at some stage in the development of new products. For similar reasons and because of the large variety of feedstock and gasification processes, it is expected that CFD will have a similar position in the design of next-generation gasifiers. Promoting the use of advanced modeling techniques such as CFD is even more justified when looking at the particular case of entrained-flow gasifiers. The feedstock delivery is performed with high gas-phase momentum (e.g. injection system with high pressure ratios). The complexity of the feedstock and of the injection sub-process yields a complex turbulent multiphase reacting flow, which is highly non-linear. The difficulty in modeling resides mainly in the fact that each subsequent sub-process, such as

* Corresponding author.
E-mail address: georg.eckel@dlr.de (G. Eckel).

https://doi.org/10.1016/j.fuel.2018.02.176
Received 10 May 2017; Received in revised form 23 February 2018; Accepted 27 February 2018

Nomenclature

Non-dimensional Numbers

Nu	Nusselt number
Pr	Prandtl number
Re	Reynolds number
Sc	Schmidt number
Sh	Sherwood number

Calligraphic symbols

$\mathscr{M}_\alpha$	reactant	[–]
$\mathscr{O}$	order of magnitude	[–]
$\mathscr{R}$	specific gas constant	$[\frac{J}{kg\,K}]$
$\mathscr{S}_{ij}^d$	tensor in the WALE model	$[\frac{1}{s^2}]$

Greek letters without a diacritical mark

Δh_{vap}	specific enthalpy of evaporation	$[\frac{J}{kg}]$
Δx,Δy,Δz	x, y, z-dimension of the mesh cell	[m]
Δ	filter width	[m]
λ	stoichiometric ratio	[–]
ν_t	kinematic turbulent viscosity	$[\frac{m^2}{s}]$
Ω	volume of the domain	[m^3]
ρ_g	gas density	$[\frac{kg}{m^3}]$
ρ_l	liquid density	$[\frac{kg}{m^3}]$
τ_t	turbulent time scale	[s]
τ_p	particle response time	[s]

Greek letters with a diacritical mark

$\overline{\Psi}$	filtered value of a quantity Ψ [–]
$\widetilde{\Psi}$	density weighted filtered value of a quantity Ψ [–]
$\nu'_{\alpha,r}$	stoichiometric coefficient of the reactant α in reaction r [–]
$\nu''_{\alpha,r}$	stoichiometric coefficient of the product α in reaction r [–]

Roman letters without a diacritical mark

A_r	constant in the Arrhenius equation	[–]
B_M	Spalding mass transfer number	[–]
b_r	temperature exponent in the Arrhenius equation	[–]
B_T	Spalding heat transfer number	[–]
B_{ij}	diffusion coefficient tensor in the dispersion model	$[\frac{m}{s^{3/2}}]$
c_d	drag coefficient	[–]
c_{p_l}	specific isobaric heat capacity of the liquid	$[\frac{J}{kg\,K}]$
C_{sgs}	model constant in the WALE model	[–]
D_α	diffusion coefficient of species α	$[\frac{m^2}{s}]$
d_p	particle diameter	[m]
e^α	specific internal energy associated with species α	$[\frac{J}{kg}]$
$E_{a,r}$	activation energy of the reaction r	[J]
G	filter function	[–]
g_{ij}	velocity gradient tensor	$[\frac{1}{s}]$
h	specific enthalpy	$[\frac{J}{kg}]$
h_α	specific enthalpy of species α	$[\frac{J}{kg}]$
K	kernel function	[–]
k_r	reaction rate of reaction r	[–]
L	characteristic length scale	[m]
m_p	mass of parcel p	[kg]
m_p	particle mass	[kg]
M_α	Molar mass of species α	$[\frac{kg}{mol}]$
N_p	number of parcels in the cell	[–]
N_{sp}	number of species	[–]
p_{atm}	ambient pressure	$[\frac{N}{m^2}]$
S_ϕ^p	source term of a single parcel p	[–]
T	temperature	[K]
t	time	[s]
T_0	reference temperature	[K]
T_g	gas temperature	[K]
T_p	particle temperature	[K]
T_g^∞	gas temperature in the farfield	[K]
T_g^S	gas temperature at the droplet surface	[K]
T_{wall}	wall temperature	[K]
V_f	filter volume	[m^3]
W	Wiener process	[–]
Y_p^α	liquid mass fraction of species α	[–]
Y_α^∞	species mass fraction in the farfield	[–]
Y_α^S	species mass fraction at the droplet surface	[–]

Roman letters with a diacritical mark

$\overline{S}_\phi^d$	filtered spray source term	[–]
$\dot{m}_{air}$	air mass flow rate	$[\frac{kg}{s}]$
$\dot{m}_{fuel}$	fuel mass flow rate	$[\frac{kg}{s}]$
$\dot{m}_{O_2}$	oxygen mass flow rate	$[\frac{kg}{s}]$
$\dot{m}_{surf}$	surface mass flow rate	$[\frac{kg}{s}]$
$\dot{Q}_{surf}$	surface heat flow rate	$[\frac{J}{s}]$
$\widetilde{S}_{ij}$	strain rate tensor of the resolved scales	$[\frac{1}{s}]$
$\vec{a}_d$	acceleration vector due to drag	$[\frac{m}{s^2}]$
$\vec{F}$	external forces	[N]
$\vec{F}_d$	drag force	[N]
$\vec{g}$	acceleration vector due to gravity	$[\frac{m}{s^2}]$
$\vec{u}_p$	particle velocity vector	$[\frac{m}{s}]$
$\vec{u}_g$	gas velocity vector	$[\frac{m}{s}]$
$\vec{u}_{rel}$	relative velocity vector	$[\frac{m}{s}]$
$\vec{x}_p$	particle position vector	[m]

atomization, turbulent dispersion, evaporation, mixing, or homogeneous and heterogeneous chemical reactions, is quasi impossible to capture with algebraic models or with correlations, which are often inaccurate and highly narrow-ranged. Only an iterative numerical method where fluid dynamics, particle dynamics, and reaction kinetics are coupled can provide an authentic and verifiable solution. Nevertheless, the prediction of physical and chemical phenomena occurring in high temperature and high pressure multiphase flow systems such as industrial entrained flow gasifiers remains a major scientific challenge even with modern CFD tools. Numericists face challenges due to the multi-scale nature of the problem, complex fuel compositions and particle topologies as well as the many sub-processes involved. Concerning the multi-scale nature, length scales for example vary from particle sizes of the order of $\mathscr{O}(1{-}100\,\mu m)$ to geometrical dimensions of the reaction chamber of the order of $\mathscr{O}(1{-}10\,m)$. Time scales differ several orders of magnitude between fast homogeneous reactions ($\mathscr{O}(10^{-3}{-}10^{-10}\,s)$) [3] and residence times of residual fly ash ($\mathscr{O}(10\,s)$). Velocities range from $\mathscr{O}(100{-}150\,m/s)$ in the injector near-field to $\mathscr{O}(0{-}1\,m/s)$ in far-field regions. The complex fuel compositions and topologies result from the fact that waste and biomass based slurries are

heterogeneous mixtures composed of immiscible liquids (emulsions) and solid non-uniform particles (suspensions). In order to reduce the complexity, experiments and numerical simulations within this study were conducted on a well-defined gas-liquid flow system with a model fuel (mono-ethylene glycol) under atmospheric but realistic flow and temperature conditions. This configuration serves as a reference avoiding the high uncertainties regarding initial slurry composition, heterogeneous reactions and related phenomena. In particular, processes inside the porous particles during gasification are not well understood, up to now [4]. The model fuel was chosen to be mono-ethylene glycol due to the fact that its chemical structure (C/H-ratio, C/O-ratio), lower heating value and physical properties are comparable to those of pyrolysis oil (details see Part 1 of this paper series [1]).

This article is the sequel to “Entrained flow gasification. Part 1: Gasification of glycol in an atmospheric-pressure experimental rig ” [1] and “Entrained flow gasification. Part 2: Mathematical modeling of the gasifier using RANS method” [2]. Using the experimental data set provided in Part 1 of the coordinated papers for validation purposes, the main focus here is on the detailed physical understanding of the near injector region of the entrained flow gasifier REGA [1]. For that purpose, more computationally intensive models are used with respect to the numerical approach presented in Part 2, which is dedicated to the development of a numerical design tool for the entire domain. Here, the turbulent flow in the continuous phase is modeled using Large Eddy Simulation (LES), the sub-processes pertaining to the discrete phase (spray) are modeled using a Lagrangian approach, and the reactions kinetics are modeled using detailed chemistry including turbulence-chemistry interaction. A 3D grid, well refined in the near injector region and adapted to LES computations captures the details of the injection system and the confined turbulent jet-flow.

Although many groups have already successfully applied LES to pulverized coal flames [5–9] and spray combustion [10–18], LES has so far hardly been used to analyze gasification. One of these rare examples can be found in [19], who presented Large Eddy Simulations of coal gasification in an entrained flow gasifier using global chemistry. To the authors’ knowledge, the paper at hand presents one of the first simulations of entrained-flow gasification combining a detailed description of turbulence (LES), spray (Lagrangian Particle Tracking) and chemistry (44 species and 329 reactions).

2. Modeling

2.1. Gas flow solver

The gaseous phase is calculated by the pressure-based DLR in-house code THETA (Turbulent Heat Release Extension of the TAU Code). THETA is a 3D finite volume solver for unstructured dual grids. The convective and diffusive fluxes are discretized using second-order central differencing schemes. The time discretization is based on a second-order Three-Point Backward (TPB) scheme. A projection method is applied to couple velocity and pressure. The Poisson equation for the pressure correction is solved by the FGMRES method preconditioned by a single multigrid V-cycle. The other transport equations are computed by the BiCGStab method with Jacobi preconditioning. In order to reduce memory requirements, a matrix-free formulation for all linear equations is used [20].

2.1.1. Large eddy simulation

The simulation of turbulence is a multi-scale problem in time and space [21] and the characteristics of large and small scales are very different [22]. The energy-rich, inhomogeneous, large scales have a longer life span and depend on the geometry. In contrast, the small scales are short-lived, dissipative and have a more isotropic, universal character [23]. Due to this fact, the basic idea of Large Eddy Simulations (LES) is to separate the large scales from the small ones by a filtering operation. The spatially filtered value $\overline{\Psi}$ of a quantity $\Psi(\vec{x},t)$ results from the convolution with the filter function G and is defined as:

$$\overline{\Psi} = \int_{\Omega} \Psi(\vec{y},t)\, G(\vec{x}-\vec{y};\Delta\vec{x})\, d\vec{y} \tag{1}$$

wherein Ω and Δ represent the entire domain and the filter width, respectively. In a finite volume formulation an implicit filtering by the discretization is often adopted and also used within this work. This leads to the following spatially varying filter width:

$$\Delta = (\Delta x \Delta y \Delta z)^{1/3} \tag{2}$$

Advantages and drawbacks of this method can be found in [23,24]. In case of density variations due to temperature changes, chemical reactions or compressibility, it is widely accepted to introduce a density weighted (Favre) filtering [25] [26] [24]. The density weighted filtered value $\widetilde{\Psi}$ of a quantity Ψ is defined as:

$$\widetilde{\Psi} = \frac{\overline{\rho_g \Psi}}{\overline{\rho}_g} \tag{3}$$

Filtering the mass conservation equation for a reacting gas-liquid mixture gives:

$$\frac{\partial \overline{\rho}_g}{\partial t} + \frac{\partial}{\partial x_i}(\overline{\rho}_g \widetilde{u}_i) = \overline{S}_{\rho}^{d} \tag{4}$$

with the filtered mass source term $\overline{S}_{\rho}^{d}$ due to the presence of the liquid droplets. Filtering the momentum conservation equation for a reacting gas mixture yields:

$$\frac{\partial}{\partial t}(\overline{\rho}_g \widetilde{u}_i) + \frac{\partial}{\partial x_j}(\overline{\rho}_g \widetilde{u}_i \widetilde{u}_j) - \frac{\partial}{\partial x_j}(\overline{\tau}_{ij} - \overline{\rho}_g(\widetilde{u_i u_j} - \widetilde{u}_i \widetilde{u}_j)) = -\frac{\partial \overline{p}}{\partial x_i} + \overline{\rho}_g f_i + \overline{S}_{\rho u}^{d} \tag{5}$$

with the filtered momentum source term $\overline{S}_{\rho u}^{d}$ due to the presence of the liquid droplets. Assuming a Newtonian fluid (linear dependence of the stresses on the shear) and replacing the volume viscosity according to the Stokes hypothesis, the filtered stress tensor in Eq. (5) has the form:

$$\overline{\tau}_{ij} = \overline{\rho}_g \nu \left(\frac{\partial \widetilde{u}_i}{\partial x_j} + \frac{\partial \widetilde{u}_j}{\partial x_i} - \frac{2}{3}\delta_{ij}\frac{\partial \widetilde{u}_k}{\partial x_k} \right) \tag{6}$$

The unresolved sub-grid Reynolds stresses $\overline{\rho}_g(\widetilde{u_i u_j} - \widetilde{u}_i \widetilde{u}_j)$ are calculated by the WALE (Wall-Adapting Local Eddy-viscosity) model [27] [28]. As the name of the model indicates, it follows the tradition of classical RANS approaches relying on the eddy viscosity concept proposed by Boussinesq [29]. By analogy with the resolved stresses caused by molecular viscosity (Eq. (6)), the eddy viscosity concept introduces a turbulent viscosity relating the unresolved sub-grid Reynolds stresses to the resolved flow:

$$\overline{\rho}_g(\widetilde{u_i u_j} - \widetilde{u}_i \widetilde{u}_j) = -\overline{\rho}_g \nu_t \left(\frac{\partial \widetilde{u}_i}{\partial x_j} + \frac{\partial \widetilde{u}_j}{\partial x_i} - \frac{2}{3}\delta_{ij}\frac{\partial \widetilde{u}_k}{\partial x_k} \right) + \frac{2}{3}\delta_{ij}\overline{\rho}_g k_{sgs} \tag{7}$$

In case of incompressible flows, the dilatational term (last term in the brackets) of Eq. (6) and Eq. (7) is zero. The very last term on the right hand side of Eq. (7) is added to ensure that the sum of the normal stresses equals $2k_{sgs}$. The eddy viscosity is modeled by:

$$\nu_t = (C_{sgs}\Delta)^2 \frac{(\mathscr{S}_{ij}^{d}\mathscr{S}_{ij}^{d})^{\frac{3}{2}}}{(\widetilde{S}_{ij}\widetilde{S}_{ij})^{\frac{5}{2}} + (\mathscr{S}_{ij}^{d}\mathscr{S}_{ij}^{d})^{\frac{5}{4}}} \tag{8}$$

This formulation is based on the traceless symmetric part of the square of the velocity gradient tensor:

$$\mathscr{S}_{ij}^{d} = \frac{1}{2}(\widetilde{g}_{ij}^{2} + \widetilde{g}_{ji}^{2}) - \frac{1}{3}\delta_{ij}\widetilde{g}_{kk}^{2} \tag{9}$$

with

$$\widetilde{g}_{ij}^{2} = \widetilde{g}_{ik}\widetilde{g}_{kj} \tag{10}$$

and the velocity gradient tensor:

$$\widetilde{g}_{ij} = \frac{\partial \widetilde{u}_i}{\partial x_j} \tag{11}$$

$\widetilde{S}_{ij}$ represents the strain rate tensor of the resolved scales:

$$\widetilde{S}_{ij} = \frac{1}{2}\left(\frac{\partial \widetilde{u}_i}{\partial x_j} + \frac{\partial \widetilde{u}_j}{\partial x_i}\right) \tag{12}$$

Within the work at hand a model constant of $C_{sgs} = 0.325$ was used [30].

In low Mach number flows the viscous dissipation $\tau_{ij}\frac{\partial u_i}{\partial x_j}$ can be neglected and the substantial derivative of pressure approximated by $\frac{Dp}{dt} \approx \frac{d\overline{p}}{dt}$ [25]. In addition, radiation was neglected within this study. This leads to the filtered enthalpy conservation equation:

$$\frac{\partial}{\partial t}(\overline{\rho}_g \widetilde{h}) + \frac{\partial}{\partial x_i}(\overline{\rho}_g \widetilde{u}_i \widetilde{h}) + \frac{\partial}{\partial x_i}(\overline{q}_i - \overline{\rho}_g(\widetilde{u_i h} - \widetilde{u}_i \widetilde{h}))) = \frac{d\overline{p}}{dt} + \overline{\rho}_g f_i \widetilde{u_i} + \overline{S}_h^d \tag{13}$$

wherein $\overline{S}_h^d$ is the enthalpy source term due to the presence of the droplets and the specific enthalpy of a gas mixture h defined as:

$$h = \sum_{\alpha=1}^{N_{sp}} h_\alpha Y_\alpha \tag{14}$$

with the specific enthalpy h_α of species α:

$$h_\alpha = \Delta h_{f,\alpha}^0 + \int_{T_0}^{T} c_{p,\alpha} dT \tag{15}$$

In Eq. (15) $h_{f,\alpha}^0$ represents the heat of formation and $c_{p,\alpha}$ the specific isobaric heat capacity of species α. The filtered energy flux $\overline{q}_i$ in Eq. (13) is assumed to be only composed of thermal conduction (Fourier's law) and energy fluxes due to species diffusion and modeled by:

$$\overline{q}_i = -\overline{\lambda}\frac{\partial \widetilde{T}}{\partial x_i} + \sum_{\alpha=1}^{N_{sp}} \widetilde{h}_\alpha \overline{j}_{\alpha i} \tag{16}$$

Filtering the species conservation equation for a reacting gas mixture results in:

$$\frac{\partial}{\partial t}(\overline{\rho}_g \widetilde{Y}_\alpha) + \frac{\partial}{\partial x_i}(\overline{\rho}_g \widetilde{u}_i \widetilde{Y}_\alpha) + \frac{\partial}{\partial x_i}(\overline{j}_{\alpha i} - \overline{\rho}_g(\widetilde{u_i Y_\alpha} - \widetilde{u}_i \widetilde{Y}_\alpha))) = \overline{S}_{Y_\alpha} + \overline{S}_{Y_\alpha}^d \tag{17}$$

The filtered species diffusion fluxes $\overline{j}_{\alpha i}$ were approximated by a formulation based on Fick's law neglecting species diffusion due to temperature gradients (thermophoresis or Soret effect) and pressure gradients as well as species diffusion induced by external forces:

$$\overline{j}_{\alpha i} = -\overline{\rho}_g \overline{D}_\alpha \frac{\partial \widetilde{Y}_\alpha}{\partial x_i} \tag{18}$$

The diffusion coefficient D_α of species α into the mixture is determined from the binary diffusion coefficients according to [31]. The filtered species source term $\overline{S}_{Y_\alpha}$ due to chemical reactions will be addressed in Section 2.1.2.

For the closure of the unresolved scalar fluxes $\overline{\rho}_g(\widetilde{u_i\phi} - \widetilde{u}_i\widetilde{\phi})$ with $\phi = h, Y_1, \ldots, Y_{sp-1}$ the widely-used gradient diffusion hypothesis was applied, i.e. the scalar transport follows the main scalar gradient [22]:

$$\overline{\rho}_g(\widetilde{u_i\phi} - \widetilde{u}_i\widetilde{\phi}) = \overline{\rho}_g \Gamma_t \frac{\partial \widetilde{\phi}}{\partial x_i} \tag{19}$$

The diffusion coefficient Γ_t was determined by means of a turbulent Prandtl number and a turbulent Schmidt number for the enthalpy and species equations, respectively. For the enthalpy equation ($\phi = h$) this leads to:

$$\Gamma_t = \frac{\nu_t}{Pr_t} \tag{20}$$

For the species equations ($\phi = Y_1, \ldots, Y_{sp-1}$) the diffusion coefficients yield:

$$\Gamma_t = \frac{\nu_t}{Sc_t} \tag{21}$$

Both the turbulent Prandtl number and the turbulent Schmidt number were set to a constant value of one. Ivanova (2012) [32] showed that the dependence of the solution on the constants chosen was minor as the resolved scalar fluxes tend to dominate the modeled (sub-grid scale) scalar fluxes.

In total, Eq. (4), Eq. (5), Eq. (13) and Eq. (17) results in a set of $N_{sp} + 4$ transport equations to be solved. The last species is calculated by:

$$\sum_{\alpha=1}^{N_{sp}} Y_\alpha = 1 \tag{22}$$

The gas density ρ_g can be calculated by the ideal gas law for a gaseous mixture:

$$\rho_g = \frac{p_g}{\mathscr{R} T_g \sum_{\alpha=1}^{N_{sp}} (Y_\alpha / M_\alpha)} \tag{23}$$

2.1.2. Chemical reactions

The detailed chemical reaction mechanism for mono-ethylene glycol consists of $N_{sp} = 44$ species and a set of $N_r = 329$ elementary reactions. These elementary reactions describe the conversion of a reactant $\mathscr{M}_\alpha$ into a product and can be generalized by the following formulation [25]:

$$\sum_{\alpha}^{N_{sp}} \nu'_{\alpha,r} \mathscr{M}_\alpha \underset{k_{b,r}}{\overset{k_{f,r}}{\rightleftharpoons}} \sum_{\alpha}^{N_{sp}} \nu''_{\alpha,r} \mathscr{M}_\alpha \tag{24}$$

with $\nu'_{\alpha,r}$ representing the stoichiometric coefficient of the reactant α in reaction r. Accordingly, $\nu''_{\alpha,r}$ represents the stoichiometric coefficient on the product side. The forward and backward reaction rate $k_{f,r}$ and $k_{b,r}$, respectively, can be calculated by the modified Arrhenius equation [33]:

$$k_r = A_r T^{b_r} exp\left(-\frac{E_{a,r}}{\mathscr{R} T}\right) \tag{25}$$

The pre-exponential factor incorporates the constant A_r and the temperature exponent b_r. $E_{a,r}$ is the activation energy of the reaction r.

In case of laminar reactive flows, the source term for species $\alpha = 1, \ldots, N_{sp}-1$ on the right hand side of Eq. (17) can be calculated by adding up the source term contributions of all elementary reactions in the chemical kinetics mechanism [25]:

$$S_\alpha = M_\alpha \sum_{r=1}^{N_r} \left((\nu''_{\alpha,r} - \nu'_{\alpha,r}) \left(k_f \prod_{\beta=1}^{N_{sp}-1} [\mathscr{M}_\alpha]^{\nu'_{\beta,r}} - k_b \prod_{\beta=1}^{N_{sp}-1} [\mathscr{M}_\alpha]^{\nu''_{\beta,r}} \right) \right) \tag{26}$$

with the concentration $[\mathscr{M}_\alpha]$ of species $\mathscr{M}_\alpha$ defined by:

$$[\mathscr{M}_\alpha] = \frac{\rho_g Y_\alpha}{M_\alpha} \tag{27}$$

In case of turbulent reactive flows, the influence of non-resolved, sub-grid scale turbulent fluctuations on chemistry has to be incorporated in a so-called sub-grid scale model for turbulence-chemistry interaction. In the work at hand, the filtered chemical source term $\overline{S}_{Y_\alpha}$ is computed by a turbulence-chemistry interaction sub-grid scale model based on an assumed probability density function approach [25]. Two additional transport equations are solved: one for the sub-grid scale temperature variance and one for the sum of the sub-grid scale species mass fraction variances. In the sub-grid scale, it is assumed that the temperature follows a clipped Gaussian pdf while the species mass fractions follow a multivariate β-pdf [31].

The reduced reaction mechanism of mono-ethylene glycol used within this part of the paper series originates from the detailed reaction

mechanism of Hafner et al. [34,35] containing 81 species and 666 elementary reactions. It includes reactions of mono-ethylene glycol with base C1-C4 chemistry. Being unimportant to the mono-ethylene glycol system, mainly reactions of the C3-C4 chemistry were removed resulting in a reduced reaction mechanism of 44 species and 329 reactions. The fuel mono-ethylene glycol is consumed mainly via decomposition reactions or by removal of H-atoms via abstraction reactions. The H-abstraction leads to fuel radicals $HOCH_2CHOH$ and $HOCH_2CH_2O$, the latter being less likely to form than the secondary fuel radical $HOCH_2CHOH$. In the fuel decomposition channel, the main reactions are the C-C bond breaking of mono-ethylene glycol resulting in two hydroxy-methyl radicals as well as the C-O and O-H bond dissociation finally reforming to acetaldehyde. Further decomposition and intermediate formation chemistry is governed by the kinetics of these species. For further details the reader is referred to [36].

2.2. Dispersed phase solver

The dispersed liquid phase is computed by the DLR in-house code SPRAYSIM, which is based on a Lagrangian particle tracking method using a point source approximation, i.e. droplets are assumed to be mathematical points providing point sources and point forces to the gas field. Lagrangian particle tracking requires solving the coupled ordinary differential equations for $\vec{x}_p$,$\vec{u}_p$,d_p and T_p along the trajectory of each computational parcel. These ordinary differential equations describe the change of the particle location, velocity, diameter as well as temperature with time [26]. The particle position is directly linked to the particle velocity and can be described by:

$$\frac{d\vec{x}_p}{dt} = \vec{u}_p \tag{28}$$

The change in particle velocity is calculated by Newton's second law summing accelerations acting on the particle:

$$\frac{d\vec{u}_p}{dt} = \vec{a}_d + \left(1-\frac{\rho_g}{\rho_l}\right)\vec{g} \tag{29}$$

with the acceleration vector due to drag $\vec{a}_d$ and due to gravity $\vec{g}$. In Eq. (29), Faxen force, Saffman force, virtual mass force, Basset force, Magnus effect, electromagnetic forces, and forces due to non-uniform evaporation were omitted, as they are negligible within the context of this study. For a spherical shape the acceleration vector due to drag can be calculated by:

$$\vec{a}_d = \frac{\vec{F_d}}{m_p} = \underbrace{\frac{3}{4}\frac{c_d}{d_p}\frac{\rho_g}{\rho_l}|\vec{u}_{rel}|}_{\tau_p^{-1}} \cdot \vec{u}_{rel} \tag{30}$$

including the drag force $\vec{F_d}$, the particle mass m_p, the drag coefficient c_d and the relative velocity $\vec{u}_{rel}$ defined as:

$$\vec{u}_{rel} = \vec{u}_g - \vec{u}_p \tag{31}$$

The reciprocal of the first term in Eq. (30) is referred to as the particle response time or particle relaxation time:

$$\tau_p = \frac{4}{3}\frac{d_p}{c_d}\frac{\rho_l}{\rho_g}\frac{1}{|\vec{u}_{rel}|} \tag{32}$$

The change in diameter d_p for a spherical particle can be derived from a mass balance:

$$\frac{d(d_p)}{dt} = -\frac{d_p}{3}\frac{1}{\rho_l}\frac{d\rho_l}{dt} - \frac{2}{\pi d_p^2}\frac{\dot{m}_{surf}}{\rho_l} \tag{33}$$

with the vapor mass flow rate $\dot{m}_{surf}$ from and to the surface of the particle in case of evaporation and condensation, respectively. In Eq. (33) the mass flow rate $\dot{m}_{surf}$ was defined to be positive in case of the former and negative in case of the latter. The change in particle temperature T_p can be deduced from an energy balance. For a spherical shape, this yields:

$$\frac{dT_p}{dt} = -\frac{6}{\pi d_p^3}\frac{\dot{m}_{surf}\Delta h_{vap}(T_p) + \dot{Q}_{surf}}{\rho_l c_{p_l}} \tag{34}$$

with the specific enthalpy of evaporation Δh_{vap}, the specific isobaric heat capacity of the liquid c_{p_l} and the surface heat flow rate $\dot{Q}_{surf}$.

2.2.1. Evaporation model

The mass flow rate $\dot{m}_{surf}$ and heat flow rate $\dot{Q}_{surf}$ from the droplet to the surrounding gas are determined by a variant of the evaporation model of Abramzon and Sirignano (1989) [37]. The evaporation rate is given by:

$$\dot{m}_{surf} = \pi d_p \rho_g D_\alpha Sh \ln(1 + B_M) \tag{35}$$

$$\dot{m}_{surf} = \pi d_p \frac{\lambda_g}{c_{p_g}} Nu \ln(1 + B_T) \tag{36}$$

In order to account for the radial Stefan flow, Abramzon and Sirignano (1989) [37] proposed a correction term for the Sherwood number Sh and the Nusselt number Nu:

$$Sh = 2 + \frac{Sh_0 - 2}{F(B_M)} \tag{37}$$

$$Nu = 2 + \frac{Nu_0 - 2}{F(B_T)} \tag{38}$$

with $F(B)$ defined by:

$$F(B) = (1 + B)^{0.7}\frac{\ln(1 + B)}{B} \tag{39}$$

and a limitation of B to the range $0 \leqslant B \leqslant 20$. B_M and B_T are the Spalding mass transfer number and Spalding heat transfer number, respectively:

$$B_M = \frac{Y_\alpha^S - Y_\alpha^\infty}{1 - Y_\alpha^S} \tag{40}$$

$$B_T = \frac{c_{p,\alpha}(T_g^\infty - T_g^S)}{\Delta h_{vap} + \frac{\dot{Q}_l}{\dot{m}_{surf}}} \tag{41}$$

The superscripts ^{S} and $^\infty$ denote values at the surface and in the far field, respectively. $\dot{Q}_l$ represents the droplet heating rate. The empirical Sherwood number Sh_0 and the empirical Nusselt number Nu_0 are calculated according to:

$$Sh_0 = 1 + (1 + ReSc)^{\frac{1}{3}} f(Re) \tag{42}$$

$$Nu_0 = 1 + (1 + RePr)^{\frac{1}{3}} f(Re) \tag{43}$$

with $f(Re)$ taken from [38]:

$$f(Re) = (max(1,Re))^{0.41-\frac{1}{3}} \quad \text{for} \quad 0 < Re < 100 \tag{44}$$

$$f(Re) = 0.752 Re^{0.472-\frac{1}{3}} \quad \text{for} \quad 100 < Re < 2000 \tag{45}$$

$$f(Re) = 0.44 Re^{\frac{1}{2}-\frac{1}{3}} + 0.034 Re^{0.71-\frac{1}{3}} \quad \text{for} \quad 2000 < Re \tag{46}$$

Equating the two equations for the surface mass flux (Eq. (35) and Eq. (36)), a relationship between the Spalding mass transfer number B_M and the Spalding heat transfer number B_T can be derived:

$$B_T = (1 + B_M)^\phi - 1 \tag{47}$$

with the exponent ϕ being:

$$\phi = \frac{Sh}{Nu}\frac{\rho_g D_\alpha c_{p,\alpha}}{\lambda_g} = \frac{Sh}{Nu\,Le} \tag{48}$$

As the value of B_T is needed to calculate Nu, an iterative method was

used to determine B_T and Nu. Finally, the droplet heating rate $\dot{Q}_l$ and the surface heat flux $\dot{Q}_{surf}$ can be calculated by:

$$\dot{Q}_l = \dot{m}_{surf}\left(\frac{c_{p,\alpha}(T_g^\infty - T_g^S)}{B_T} - \Delta h_{vap}\right) \tag{49}$$

$$\dot{Q}_{surf} = \dot{m}_{surf}\left(\frac{c_{p,\alpha}(T_g^\infty - T_g^S)}{B_T}\right) \tag{50}$$

2.2.2. Sub-grid scale model

As can be seen from Eqs. (29)–(31), the droplet trajectory depends on the relative velocity between droplet and surrounding gas. Due to droplet sizes being generally smaller than the grid size and hence the filter width, the gas velocity seen by the droplet is composed of resolved and unresolved (sub-grid) scales. The influence of the unresolved turbulent fluctuations in the sub-grid scale on the droplet dispersion is modeled by a variant of the dispersion model of Bini and Jones (2008) [39]. In this model, the droplet acceleration due to the resolved scales is equivalent to Eq. (29). Besides this deterministic part, an additional stochastic term is added to account for the unresolved sub-grid scales. Introducing the particle response time described in Eq. (32), this leads to:

$$\frac{d\vec{u}_p}{dt} = \underbrace{\frac{\vec{\tilde{u}}_g - \vec{u}_p}{\tau_p}}_{\text{resolvedscales}} + \left(1 - \frac{\rho_g}{\rho_l}\right)\vec{g} + \underbrace{\frac{\vec{u}_g - \vec{u}_p}{\tau_p}\chi}_{\text{unresolvedscales}} \tag{51}$$

Assuming the effect of the sub-grid scale fluctuations on the particle trajectory resembles a diffusion-like process similar to Einstein's formulation for Brownian motion, the diffusion process can be expressed in terms of a Wiener process [40]. Thus, an infinitely small particle velocity increment yields:

$$d\vec{u}_p = \underbrace{\frac{\vec{u}_g - \vec{u}_p}{\tau_p}\,dt + \left(1 - \frac{\rho_g}{\rho_l}\right)\vec{g}\,dt}_{\text{deterministicterms}} + \underbrace{\frac{\vec{u}_g - \vec{u}_p}{\tau_p}\,dt + \left(1 - \frac{\rho_g}{\rho_l}\right)\vec{g}\,dt\mathbf{B}\cdot d\vec{W}}_{\text{stochasticterm}} \tag{52}$$

The stochastic part on the right hand side of Eq. (52) is composed of a diffusion coefficient tensor **B** multiplied by a three-dimensional Wiener process. A time discretized Wiener process can be approximated by a series of random walks:

$$W(t_n) \approx \sqrt{\delta t}\sum_{i=1}^{n}\xi_i \tag{53}$$

with the accumulated time $t_n = n\,\delta t$ after n time steps δt as well as a random variable ξ with zero mean and a variance of unity. The diffusion coefficient tensor **B** depends on the unresolved gas velocity fluctuations $\widetilde{u_i u_j} - \tilde{u}_i\tilde{u}_j$ (Eq. (7)) and on a characteristic time scale τ_t describing the interaction between the droplet and these turbulent structures:

$$B_{ij} = \frac{\widetilde{u_i u_j} - \tilde{u}_i\tilde{u}_j}{2/3\,k_{sgs}} \cdot \sqrt{\frac{C_0}{\tau_t}k_{sgs}} \tag{54}$$

where C_0 is a model constant with a value of unity in the work at hand. The characteristic time scale τ_t is modeled by:

$$\tau_t = \tau_p^{2\alpha}\left(\frac{\sqrt{k_{sgs}}}{\Delta}\right)^{2\alpha-1} \tag{55}$$

The effect of the unresolved temperature fluctuations on the vaporization is neglected.

2.2.3. Spray source terms

Due to the presence of the spray, additional source terms for mass, momentum, energy, and species arise on the right hand side of Eq. (4), Eq. (5), Eq. (13) and Eq. (17), respectively. The filtered source terms result from the contribution S_ϕ^p of each individual parcel p located at $\vec{x}_p$ [41]:

$$\overline{S}_\phi^d(\vec{x},t) = \int_\Omega S_\phi^p(\vec{x},t)\,\delta(\vec{x}_p - \vec{x})\,G(\vec{x} - \vec{y};\Delta\vec{x})\,d\vec{y} \tag{56}$$

with the Dirac delta function $\delta(\vec{x}_p - \vec{x})$ limiting the source term to the parcel's position $\vec{x}_p$. For a top-hat or box filter like the implicit filtering by the discretization used within this work, the exact solution for the filtered source terms can be stated as:

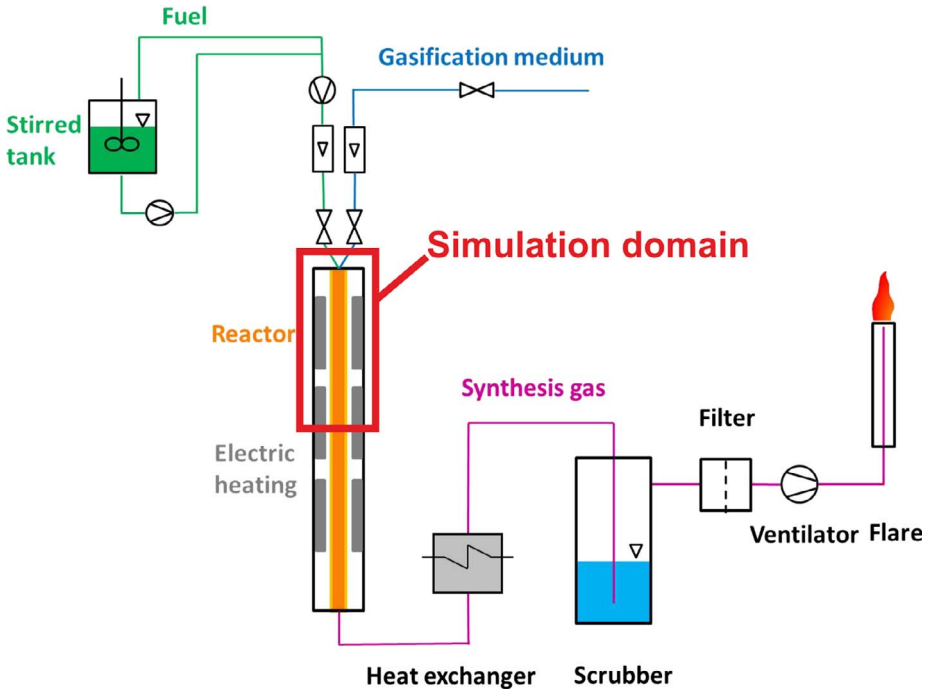

Fig. 1. Simulation domain (Schematic of the experimental setup from [1]).

$$\overline{S}_{\phi}^{d}(\vec{x},t) = \frac{1}{V_f}\sum_{p=1}^{N_p} S_{\phi}^{p}(\vec{x},t) \tag{57}$$

This represents the volume-average of N_p parcels in the filter volume V_f. In case of implicit filtering by the discretization, the filter volume V_f is equivalent to the cell volume V_{cell}. The mass change of the particles due to evaporation or condensation leads to a mass source or sink term in the gas field equations:

$$\overline{S}_{\rho}^{d}(\vec{x},t) = -\frac{1}{V_f}\sum_{p=1}^{N_p}\frac{dm_p}{dt} \tag{58}$$

$$\overline{S}_{Y_\alpha}^{d}(\vec{x},t) = -\frac{1}{V_f}\sum_{p=1}^{N_p}\frac{d(m_p Y_p^{\alpha})}{dt} \tag{59}$$

with the mass m_p of the parcel p and the liquid mass fraction Y_p^{α} of species α. A momentum source term arises due to changes in the parcel's momentum along its trajectory and due to forces acting on the parcel during a gas flow time step:

$$\overline{S}_{\rho u}^{d}(\vec{x},t) = -\frac{1}{V_f}\sum_{p=1}^{N_p}\left(\frac{d(m_p\vec{u}_p)}{dt} - \vec{F}\right) \tag{60}$$

wherein $\vec{u_p}$ represents the particle velocity vector and the second term in Eq. (60) accounts for external forces $\vec{F}$ affecting the particle, e.g. the gravity force $\vec{F_g} = m_p\vec{g}$. The energy source term yields:

$$\overline{S}_{h}^{d}(\vec{x},t) = -\frac{1}{V_f}\sum_{p=1}^{N_p}\left(\sum_{\alpha=1}^{N_{sp}}\frac{d(m_p Y_p^{\alpha} e^{\alpha})}{dt} + \frac{d(\frac{1}{2}m_p|\vec{u}_p|^2)}{dt} - \vec{F}\cdot\vec{u}_p\right) \tag{61}$$

The first term on the right hand side of Eq. (61) is the change of internal energy e, the second term the change of kinetic energy and the third one the work of external forces acting on the particle. The data are exchanged online between the gaseous Eulerian phase and the liquid Lagrangian phase via an iterative two-way-coupling procedure.

3. Test case and numerical setup

The testcase is the Research Entrained flow Gasifier (REGA) of the Karlsruhe Institute of Technology, Institute for Technical Chemistry (details see Part 1 of this paper series [1]). The atmospheric gasifier consists of a tubular reactor with a length of 3.0 m and an inner diameter of 0.28 m. The liquid fuel (mono-ethylene glycol) is injected at the top of the reactor via a twin-fluid atomizer [42]. The oxidizer consists of oxygen-enriched air and serves as atomizing agent. Flanges and an axially movable burner allow for either intrusive or optical measurements at different downstream distances from the nozzle exit. The side walls of the reactor are maintained at a constant temperature by an electric heater. The simulation domain, highlighted in Fig. 1, was discretized by a fully unstructured tetrahedral mesh. The grid was refined within the injector vanes, in the vicinity of the flame, and in near wall regions. This led to a grid size of 2.7 million points corresponding to 15.9 million volume elements. Table 1 lists the boundary conditions used in the LES of the REGA-glycol-T1 experiment. The input streams were defined according to the set point defined in Table 4 of Part 1 of this paper series [1]. The purge nitrogen was neglected. Furthermore, the leakage air, which was determined by balancing (see Part 1) after the LES was almost completed, was not considered in this computation. This leads to slightly differing boundary conditions compared to Part 2 [2] of this paper series. The starting conditions for the droplets were derived from Phase Doppler Anemometry (PDA). The twin-fluid atomizer produces a full cone spray. The droplet velocity and the liquid mass flow rate peak at the center and decrease towards larger radii. Details concerning the spray characterization can be found in Part 1 of this paper series [1]. The graphs indicate a slight w-shape and a Sauter mean diameter ranging from 60 to 80 μm. As measurements close to the atomizer are difficult because of the dense spray as well as non-spherical droplets and ligaments [43], the PDA was performed 50 mm downstream of the nozzle. However, the simulations require droplet starting conditions close to the nozzle exit as the heat-up of the spray strongly influences the position of the reaction zone. Hence, the measured profiles (50 mm downstream) were projected to a starting plane 3 mm away from the nozzle exit plane, using the intercept theorem. In this starting plane, the starting positions of the droplets were randomly generated during run-time. The characteristic droplet diameters, velocities and mass flow rates at the starting positions were obtained by linear interpolations between the experimental values at the projected points. As PDA measurements of the absolute mass flow rate have high uncertainties [43], the local mass flow rate was determined by using the relative information obtained by PDA in conjunction with the total mass flow rate supplied by the mass flow controller. An automated fitting routine was used to determine the optimum size distribution based on the characteristic diameters for each starting location. This resulted in a log-normal distribution close to the centerline and a log-Rosin-Rammler distribution towards larger radii. The quality of this procedure was verified by a comparison of the droplet size distribution for the entire spray illustrated in Fig. 2. Red bars represent the measured droplet size distribution. The blue line shows the droplet size distribution resulting from the summation of the fitted droplet size distributions of the individual starting positions. Despite the excellent agreement, it should be noted that this procedure of setting spray boundary conditions is based on approximation and introduces errors as detailed information at the location of interest is not available.

4. Numerical results, comparison and analysis

4.1. Overall flow features

The fuel is injected at the top of the gasifier. Disrupted and accelerated by the surrounding high-velocity oxidizer jet, the spray disperses in the reaction chamber interacting with turbulent structures (Fig. 3). While dispersing, the spray is heated up by the high gas temperature in the combustion region and starts to vaporize. The droplets reduce in size until they are completely evaporated. Under the present conditions, the bigger mono-ethylene glycol droplets finish evaporating in the range 600–800 mm.

4.2. Axial velocity and temperature fields

As the high-velocity oxidizer stream passes the nozzle exit, vortices are shed from the sharp corner of the injector. This can be seen in Fig. 4a, where the contour plot of the instantaneous axial velocity in the center plane is displayed, with streamlines also plotted in the right-hand half. The time-averaged axial velocity (Fig. 4b) shows the vortex street forming a large recirculation zone. It reaches 0.8 m downstream of the nozzle and covers the entire radial direction from the jet center to the confinement of the reactor. Fig. 4 shows how the simulation takes full advantage of the LES features in the near injector region. At the length and time scales defined by the injector geometry and the

Table 1
Boundary conditions used in the LES of the REGA-glycol-T1 experiment (set point defined in Table 4 of [1]).

Fuel		Mono-ethylene glycol
Gasification medium		O_2-enriched air
Fuel mass flow rate	$\dot{m}_{fuel}$	12.56 kg/h
Mass flow rate of air	$\dot{m}_{air}$	9.05 kg/h
Oxygen mass flow rate	$\dot{m}_{O_2}$	7.11 kg/h
Stoichiometric ratio	$\lambda_{tech}/\lambda_{abs}$	0.57/0.69
Pressure	p_{atm}	1.0 bar
Wall temperature	T_{wall}	1468.15 K

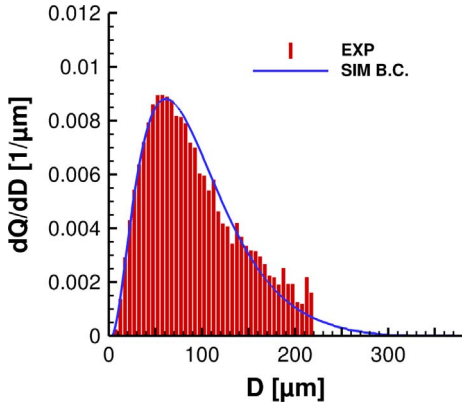

Fig. 2. Comparison of the measured (red bars) and fitted (blue line) volumetric droplet size distributions for the entire spray.

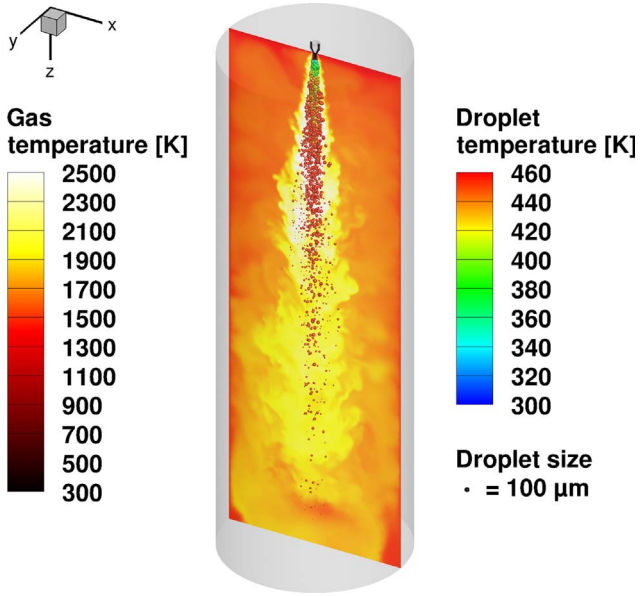

Fig. 3. Droplet dispersion and heat up.

incoming mass flow rate, the LES turbulence model captures the development of coherent structures. These coherent structures result very rapidly in a highly unsteady turbulent mixing-layer and contribute substantially to the local mixing between the incoming enriched air, the recirculating syngas, and the liquid fuel droplets. The time-averaged axial velocity (Fig. 4b) is characterized by length and time scales closer to the integral scales of the reactor, thus closer to what one could expect from a RANS turbulence model (see Part 2 of this paper series). At integral scales, the confined turbulent jet-flow is the main driver of the recirculation, which brings the gaseous components stemming from the chemical reactions along the jet axis back into the near injector region. Although the details of the twin-fluid atomizer (injection of liquid in the middle and surrounding enriched-air impinging upon it [42]) depart from a classical confined jet, from a fluid dynamics perspective the flow generated downstream the injector is qualitatively similar to it. The Reynolds number based on the hydraulic diameter of the nozzle and the average velocity through the nozzle annulus is equal to 28,800 (turbulent). Fig. 5 depicts the instantaneous (Fig. 5a) and time-averaged (Fig. 5b) temperature field in the center plane of the reaction chamber. From the flow patterns and the temperature field, five zones characterizing the near field of the injector can be defined:

1. Jet-flow along the axis close to the injector ($0 < z < 0.1$ m): This region is the potential core of the jet, which expands radially and entrains the surrounding fluid. It is characterized by a high velocity of 110 m/s and by relatively low temperatures of $300 < T < 1500$ K.
2. Jet-flow along the axis further downstream from the injector ($0.1 < z < 0.4$ m): This region is characterized by a reduced axial velocity of $40 <$ z-velocity < 100 m/s, with respect to the near injector jet region and high temperatures of $T > 2100$ K.
3. Transition region where the jet goes from occupying nearly half to almost the entire reactor cross-Section ($0.4 < z < 0.8$ m). This region is characterized by moderate axial velocities of $10 <$ z-velocity < 40 m/s and relatively high temperatures of $1500 < T < 2100$ K.
4. Mixing-layer, which is the thin layer surrounding the incoming jet close to the injector. This region is characterized by high velocity gradients and high temperatures ($T > 2100$ K).
5. Recirculation zone (see streamlines in Fig. 4b). This region is characterized by low velocities (e.g. high residence time) and by an average temperature of around 1500 K.

This definition will assist the analysis of the different reaction zones as well as the flame stabilization mechanism later on.

4.3. Vapor distribution

Mono-ethylene glycol is injected at ambient temperature (300 K). The phase transition from liquid to gas occurs along the expanding jet (Zone 1, 2, and 3). While the majority of the fuel evaporates in the preheat zone (Zone 1) as the temperature rises, larger droplets survive and reach Zone 2 and 3. This results in the mono-ethylene glycol vapor distribution shown in Fig. 6a for an instantaneous snapshot and Fig. 6b for the time-averaged field; both in the center plane and superimposed on the temperature field of Fig. 5. The instantaneous vapor distribution (Fig. 6a) and consumption rates (Fig. 6c) demonstrate that predominant length scales differ among the zones defined above. While Zone 1 is densely populated, these fields have a discrete character in Zone 2. This is related to the fact that they stem from the discrete numerical parcels representing the evaporating liquid droplets. It should be noted that the lower cut-off value for the vapor mole fraction is arbitrarily chosen to illustrate the vapor coming from the surviving droplets. Furthermore, the color scale of all figures displaying the production rate (in red) and the consumption rate (in blue) (Fig. 6c to Fig. 12c) was adjusted to emphasize details. Consequently, the intensity of the blue or red cannot be directly correlated to the instantaneous mole fractions displayed on the far left of each series.

4.4. Main reaction paths and species distributions

Ethylene glycol has to decompose before reacting. The decomposition reactions consuming the mono-ethylene glycol (Fig. 6c) lead to the formation of hydrogen (Fig. 8c) and carbon monoxide (Fig. 9c). Carbon monoxide (CO) is formed as mono-ethylene glycol ($HOCH_2CH_2OH$) decomposes to acetaldehyde (CH_3CHO) in a thermal major decomposition reaction $HOCH_2CH_2OH \rightarrow CH_3CHO + H_2O$. The acetaldehyde (Fig. 7) is then converted to CH_3CO by H-abstraction reactions which further decomposes to CO (and CH_3). Similarly, CH_2OH is formed in a second major mono-ethylene glycol decomposition reaction ($HOCH_2CH_2OH \rightarrow 2\,CH_2OH$). This species is another source of CO through reactions with oxygen O_2 or H-abstraction reactions following the pathway $CH_2OH \rightarrow CH_2O \rightarrow CHO \rightarrow CO$. Although concentrations of intermediate species, e.g. acetaldehyde (Fig. 7), are comparatively low, they are significant for the individual reaction paths leading to the formation of the main species. For example, water can be directly formed from the decomposition of mono-ethylene glycol prior to any oxidation reaction. The main sources of hydrogen (H_2) are the decomposition reaction of mono-ethylene glycol to glycolaldehyde $HOCH_2CH_2OH \rightarrow HOCH_2CHO + H_2$ and the H-abstraction reactions of

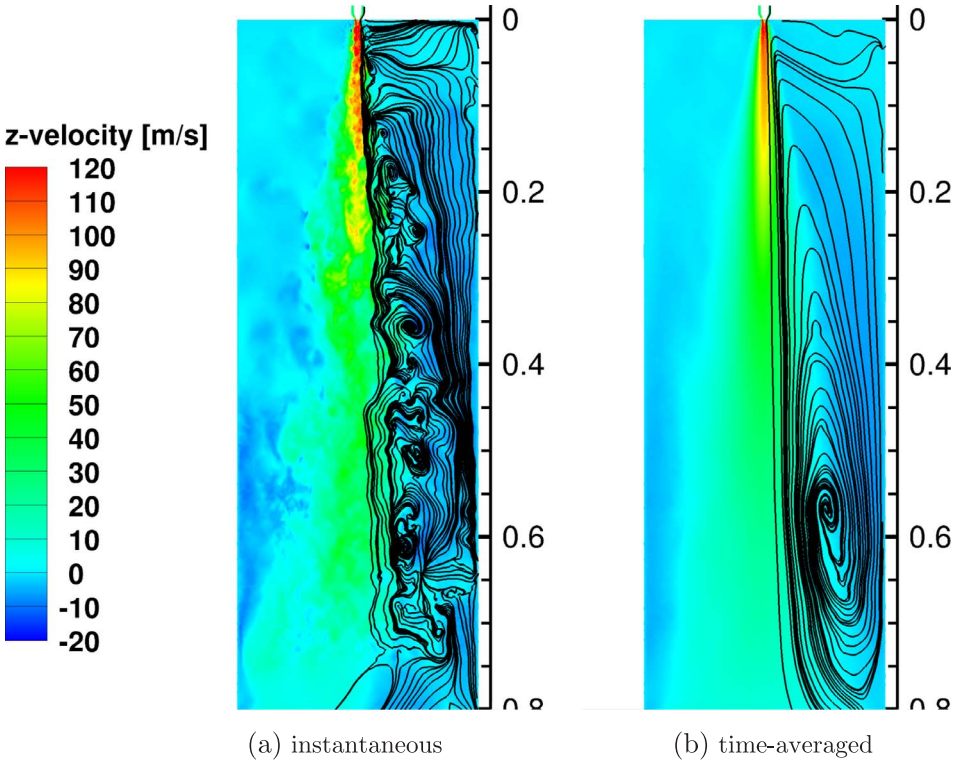

Fig. 4. Flow field.

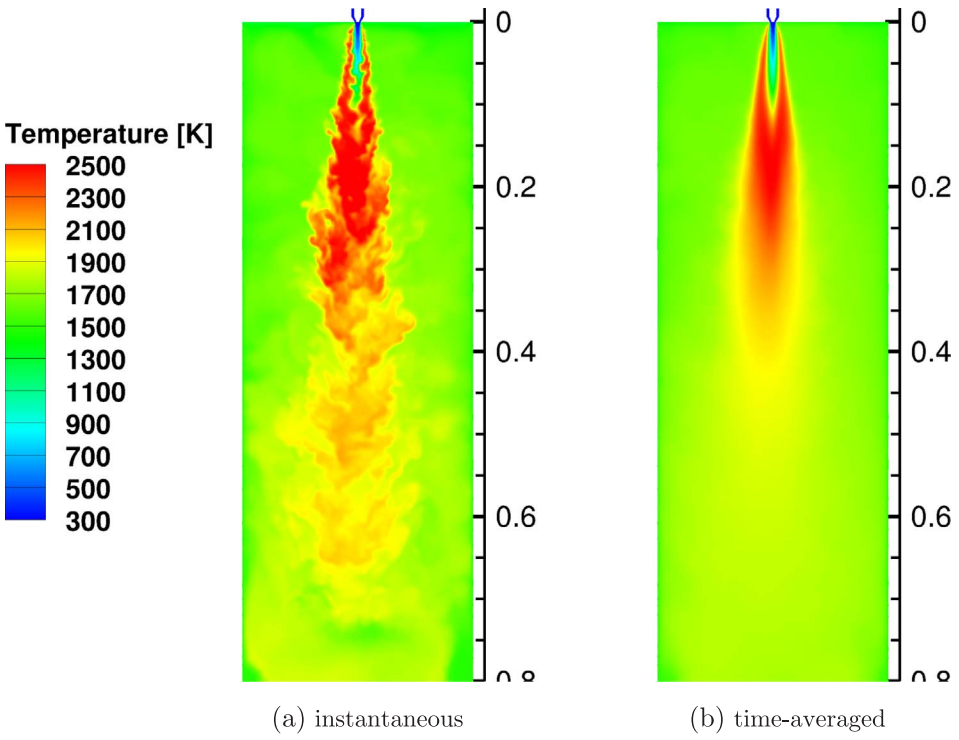

Fig. 5. Temperature field.

acetaldehyde $CH_3CHO + H \rightarrow CH_3CO + H_2$. In regions of high temperatures, hydrogen can be additionally produced by $CH_2O + H \rightarrow HCO + H_2$. As can be seen in Fig. 8c and Fig. 9c, carbon monoxide and hydrogen,i.e. the syngas, are mainly produced on the jet axis (Zone 1 and Zone 2) of the reactor. Precisely, the syngas is produced at the edge of the jet core in Zone 1 and also within Zone 2, at the scale of the liquid spray (see red dots characterizing the production along the axis in Fig. 8c and 9c). This demonstrates that the syngas stems directly from the decomposition of the mono-ethylene glycol droplets. Thereafter, CO and H_2 are transported back upstream by the recirculating flow in Zone 5. This results in the distribution of H_2 and CO illustrated in Fig. 8a, 8b and Fig. 9a, 9b, respectively. As the recirculated syngas encounters and mixes with the oxygen-rich region close to the injector, Zone 1 (Fig. 10), hydrogen and oxygen

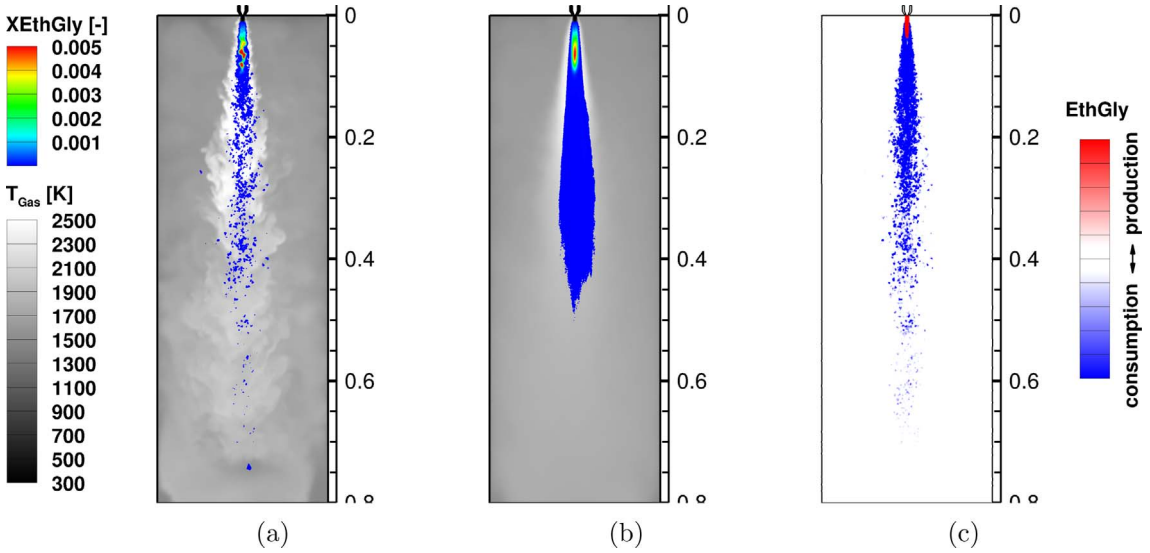

Fig. 6. Instantaneous (a) and time-averaged (b) distribution of mono-ethylene glycol superimposed on temperature field as well as instantaneous net production/ consumption rate (c) of mono-ethylene glycol.

immediately react (see consumption of O_2 in Fig. 10c, especially in the mixing-layer region) to water in a thin layer wrapping the area of high oxygen concentration (Fig. 11). The recirculated carbon monoxide reacts with the oxygen forming CO_2 (Fig. 12). The water production on the centerline within the first 0.1 m (Fig. 11c) originates directly from the fuel and is a result of the decomposition reaction of mono-ethylene glycol to acetaldehyde described above. Comparing Fig. 8c, 9c, 11c and 12c, inverted regions of production and consumption can be observed. This is a consequence of the elementary reactions summing up to the homogeneous water-gas shift reaction $CO + H_2O \rightleftharpoons CO_2 + H_2$. The equilibrium of this chain of elementary reactions is highly temperature dependent, i.e. the equilibrium constantdecreases with an increase in temperature [44]. Hence, with rising temperature the equilibrium is shifted towards the water gas (CO and H_2O) and vice versa. More specifically in the mixing-layer, the inverted regions correspond to a competition between oxidation reactions and water-gas shift reactions. When locally and temporarily there is no O_2 to mix with H_2, then the abundant H_2 delivered by the recirculating flow reacts with the CO_2 stemming from the CO oxidation. This can be seen in the thin outer sublayer of the mixing-layer, which is colored red in Fig. 9c (CO production) and colored blue in Fig. 12c (CO_2 consumption).Then, further inside the mixing-layer, CO is being consumed through the oxidation reaction thus colored blue in Fig. 9c and CO_2 is being produced thus colored red in Fig. 12c. In summary, due to the competing effect of the CO oxidation reaction and the water-gas shift reaction, there is a non-uniform and temporally alternating production and consumption of CO and H_2O in the radial as well as axial directions. These are slightly discernible in the instantaneous contour plots (Fig. 9a and Fig. 11a) but are smoothed out in the averaged field (Fig. 9b and Fig. 11b). The temperatures and fluid dynamic time scales in each separate sub-region determine which reaction prevails showing the importance of such detailed computations.

4.5. Flame stabilization mechanism

The high temperature region (Fig. 5), which builds up from the early stages of the developing mixing-layer, close to the injector (Zone 4), cannot be explained by a direct reaction of the fuel with the oxidizer. The syngas recirculation and the subsequent syngas oxidation reactions occurring in the mixing-layer, as described above, stabilize the flame.

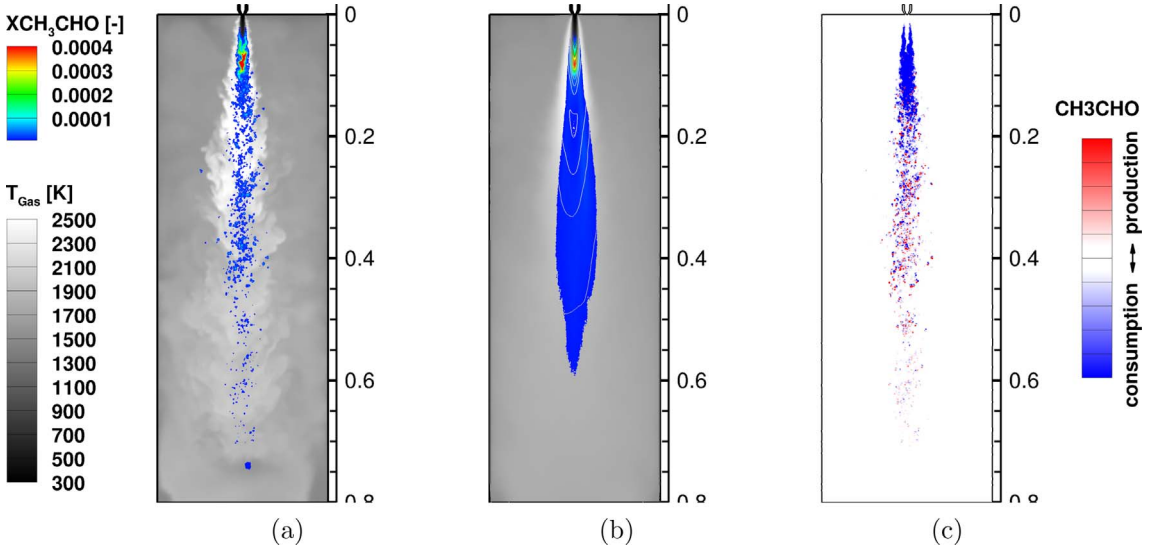

Fig. 7. Instantaneous (a) and time-averaged (b) distribution of CH_3CHO superimposed on temperature field as well as instantaneous net production/consumption rate (c) of CH_3CHO.

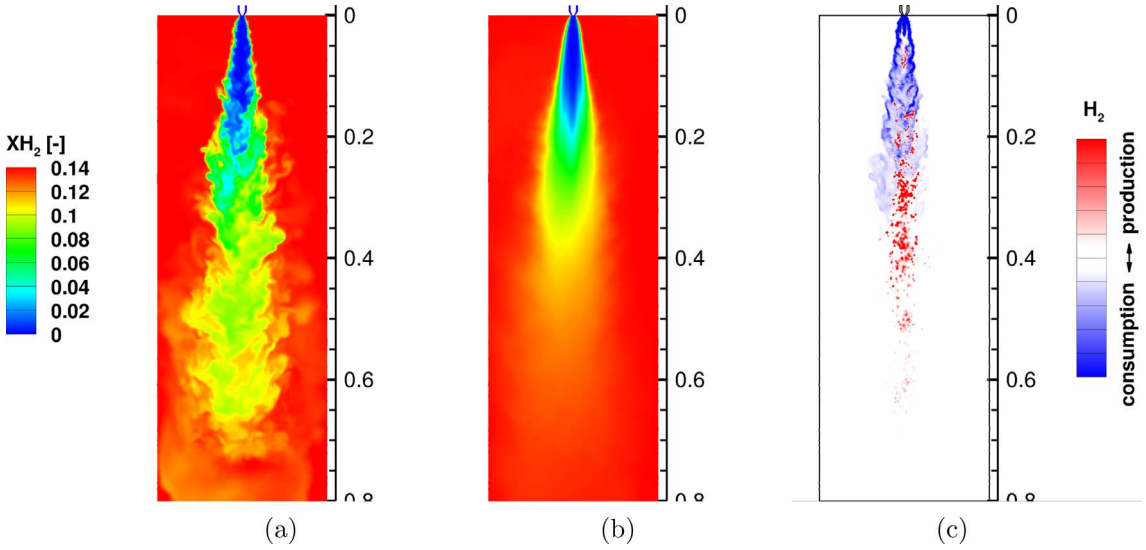

Fig. 8. Instantaneous (a) and time-averaged (b) distribution as well as instantaneous net production/consumption rate (c) of H_2.

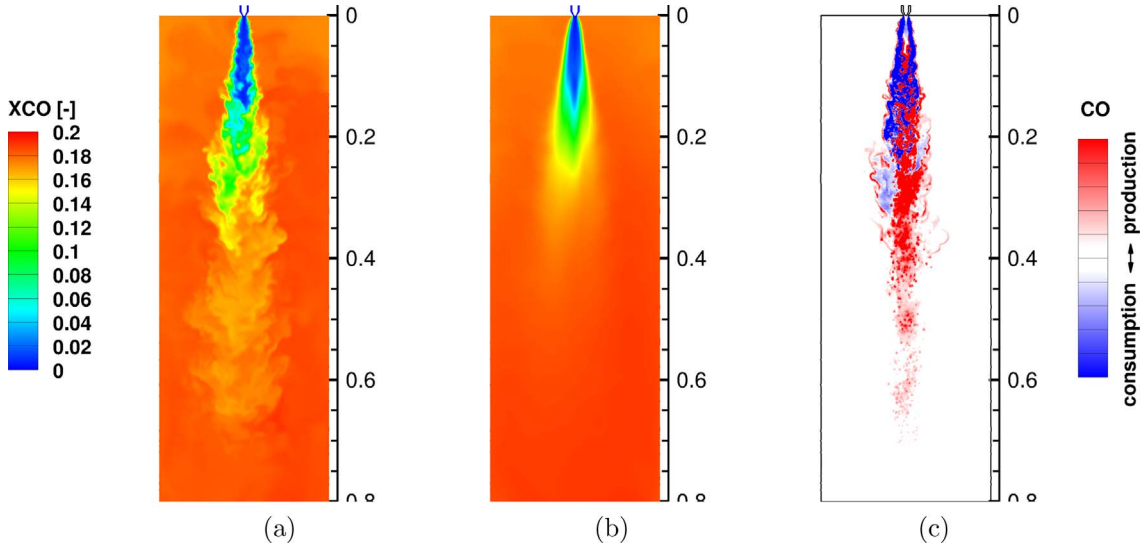

Fig. 9. Instantaneous (a) and time-averaged (b) distribution as well as instantaneous net production/consumption rate (c) of *CO*.

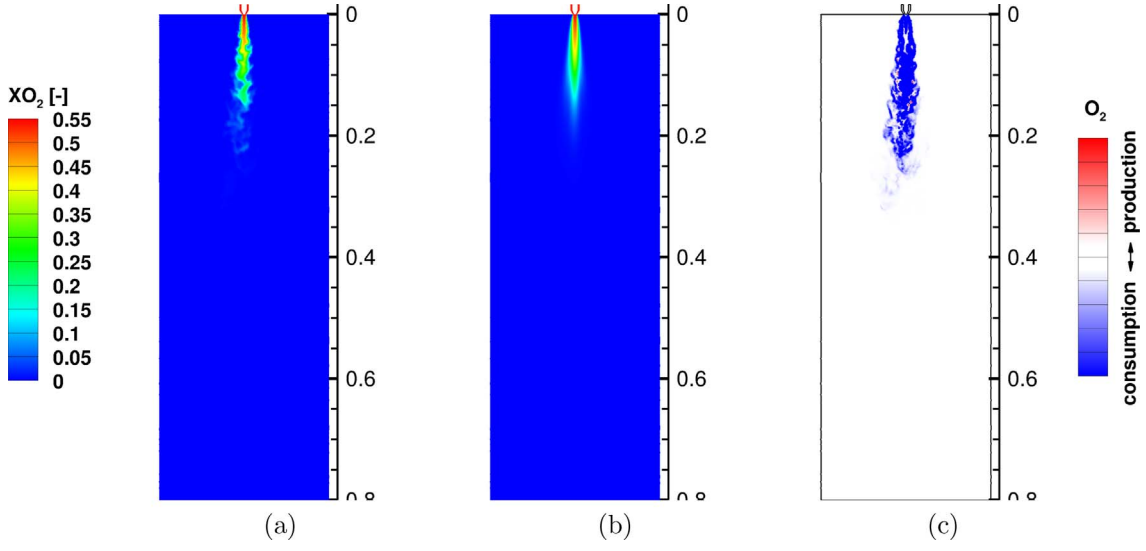

Fig. 10. Instantaneous (a) and time-averaged (b) distribution as well as instantaneous net production/consumption rate (c) of O_2.

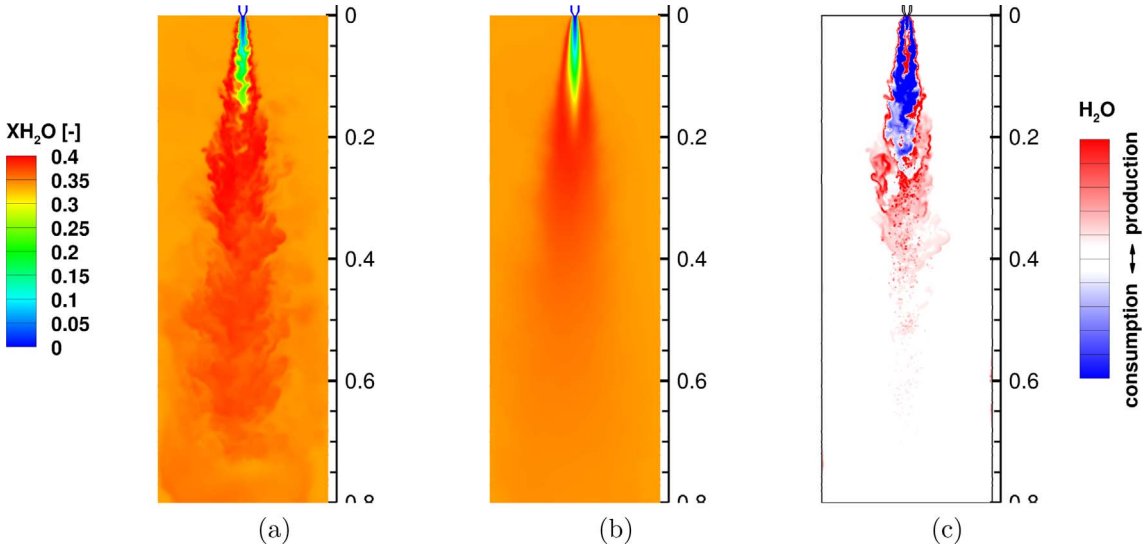

Fig. 11. Instantaneous (a) and time-averaged (b) distribution as well as instantaneous net production/consumption rate (c) of H_2O.

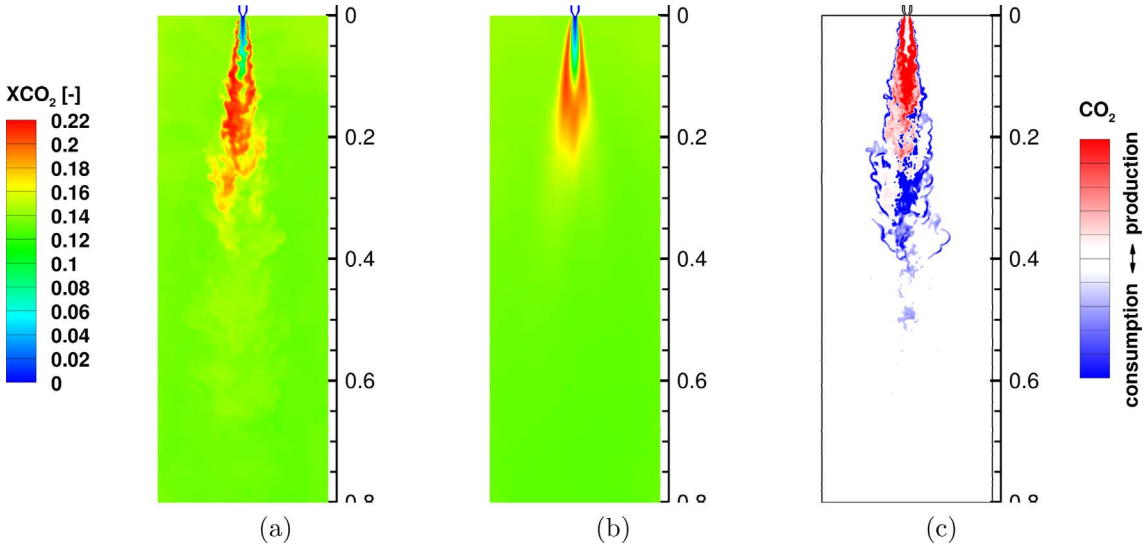

Fig. 12. Instantaneous (a) and time-averaged (b) distribution as well as instantaneous net production/consumption rate (c) of CO_2.

Flames anchored very close to the injector tip can be detrimental to the integrity and durability of the burner. This should be investigated when up-scaling the reactor and defining the fuel composition/morphology.

4.6. Temperature and species profiles

Fig. 13 and Fig. 14 show the time- and angular-averaged radial temperature and species distributions, respectively. The downstream positions, where the profiles were extracted, are depicted in Fig. 13a and Fig. 14a. The scenario described above by means of the contour plots is also reflected in the temperature and species line plots. Close to the injector the local excess of oxidizer leads to an immediate reaction of the recirculated gas with the oxygen (Fig. 13b) resulting in high temperatures at the flanks of the oxidizer jet while the jet center remains at the inflow temperature (Fig. 14b). As the oxygen is more and more consumed further downstream, the elementary reactions summing up to the homogeneous water-gas shift reaction gain in importance (see H_2 and CO_2 mole fractions). At a downstream distance of about 0.2 m, the unsteadiness of the system and the resultant enhanced mixing as well as diffusion processes cause both temperature and species to smooth out until the distributions in Fig. 13h and 14h are reached being close to equilibrium. While a good agreement between experiment and simulation can be observed in terms of temperature trends, the absolute temperature was slightly overestimated in the simulation (Fig. 13g and 13h). Small discrepancies can also be observed with respect to the species distributions (Fig. 14g and 14h). The differences may be due to two effects. Firstly, the inspection windows at the flanges were equipped with a purging system. Secondly, the balancing, presented in Part 1 of this paper series, revealed that infiltration air entered the gasifier at an unknown entry point. Both the purging medium, i.e. nitrogen (0.64 kg/h), and the infiltration air (1.93 kg/h) were not considered in the computations presented in this paper. Equilibrium calculations accounting for the purge nitrogen and the infiltration air showed a negligible effect on temperature ($\Delta T = 15$ K) but an impact on the mole fractions showing a decrease in CO ($\Delta X_{CO,N_2-free} = -2.8\%$) and H_2 ($\Delta X_{H_2,N_2-free} = -5.2\%$) mole fractions as well as an increase in CO_2 mole fraction ($\Delta X_{CO_2,N_2-free} = 8.2\%$). As a consequence, the deviations in the species mole fractions shown in Fig. 14h could be attributed to differences in the boundary conditions due to the neglected purging agent and the leakage of the experimental setup. Nevertheless, uncertainties related to the chemical kinetics mechanism used within this study can not be excluded.

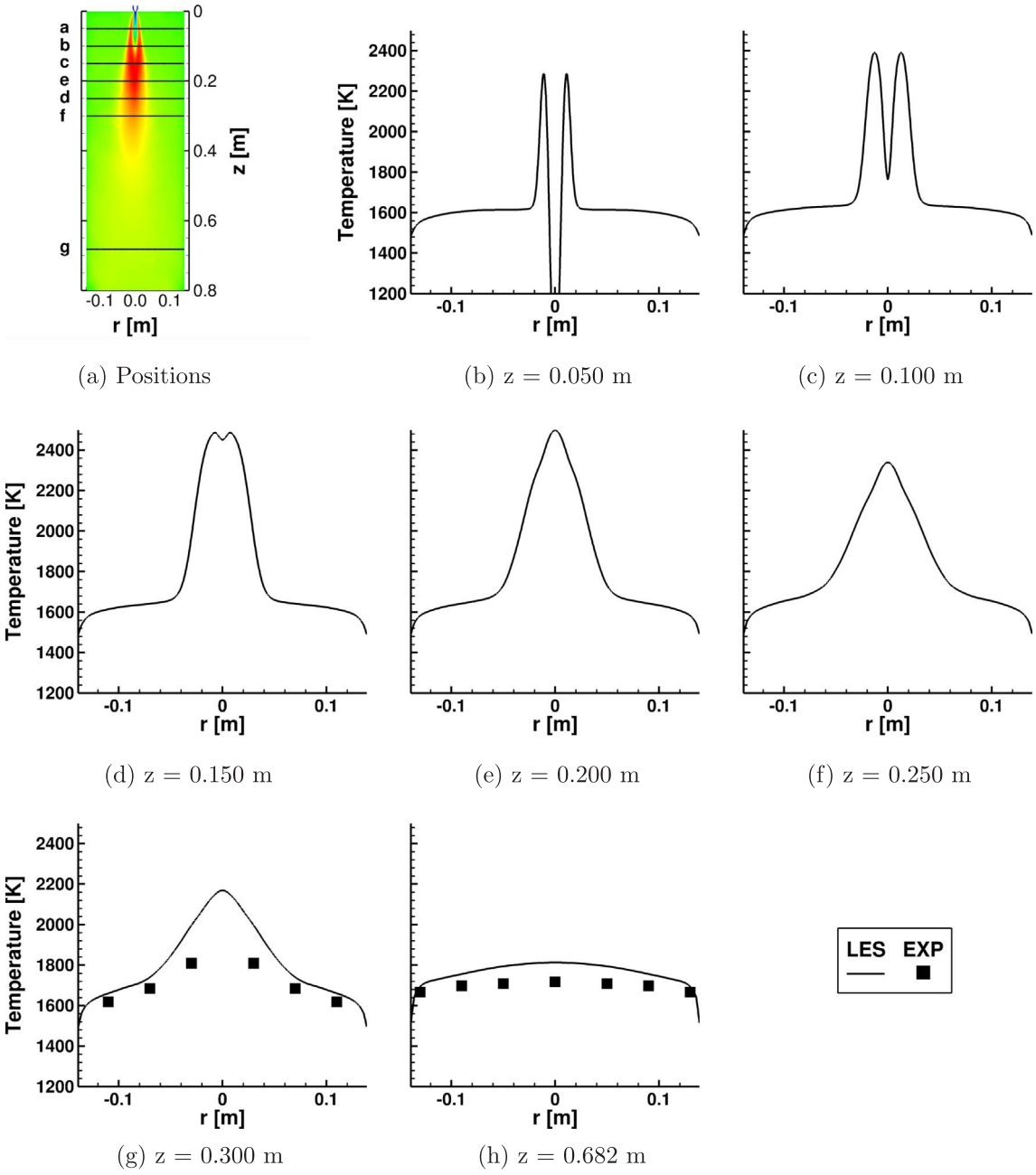

(a) Positions (b) z = 0.050 m (c) z = 0.100 m

(d) z = 0.150 m (e) z = 0.200 m (f) z = 0.250 m

(g) z = 0.300 m (h) z = 0.682 m

Fig. 13. Time- and angular-averaged radial temperature distribution (b)–(h) at the downstream positions depicted in (a): LES (lines) and experimental data (squares).

5. Conclusions and outlook

Entrained flow gasification is a promising process for the conversion of low-grade feedstock, e.g. highly viscous slurries and suspensions with a significant content of solid particles, to high quality fuels. A major scientific challenge is the prediction of the physical and chemical phenomena occurring in such high-temperature and high-pressure multiphase flow systems. In order to reduce complexity, this study focused on a two-phase (gas and liquid) flow system with a model fuel (mono-ethylene glycol) under atmospheric conditions. The unsteady flow and the chemical conversion in the gasifier were investigated by means of Large Eddy Simulations with a detailed chemistry solver directly computing the transport of 44 individual species and 329 chemical reactions. The dispersed phase was solved by Lagrangian Particle Tracking. Downstream comparisons with experimental data showed a reasonable agreement concerning temperature and species profiles. The analysis of the injector near-field revealed that the high temperature reaction zone close to the injector could not be explained by a direct reaction of the fuel with the oxidizer. Instead, carbon monoxide and hydrogen mainly formed on the axis were transported upstream by the recirculation zone. The reactions of CO and H_2 with the oxygen stabilized the flame. The heat release from this reactions supported the vaporization and decomposition of fuel as well as the downstream gasification reactions. The investigations presented in this paper series helped to gain insight into rich-burn and gasification. Regarding this as a first step, the focus will be shifted in the future from a single-component model fuel towards real fuels. This implies an increase in complexity to the point of waste and biomass based slurries. More research is needed to incorporate the complex fuel compositions and topologies into numerical tools in order to improve the predictive capabilities of the simulation. Moreover, further examinations regarding chemical kinetics under fuel-rich conditions are advisable as most of the mechanisms were derived and optimized for combustion.

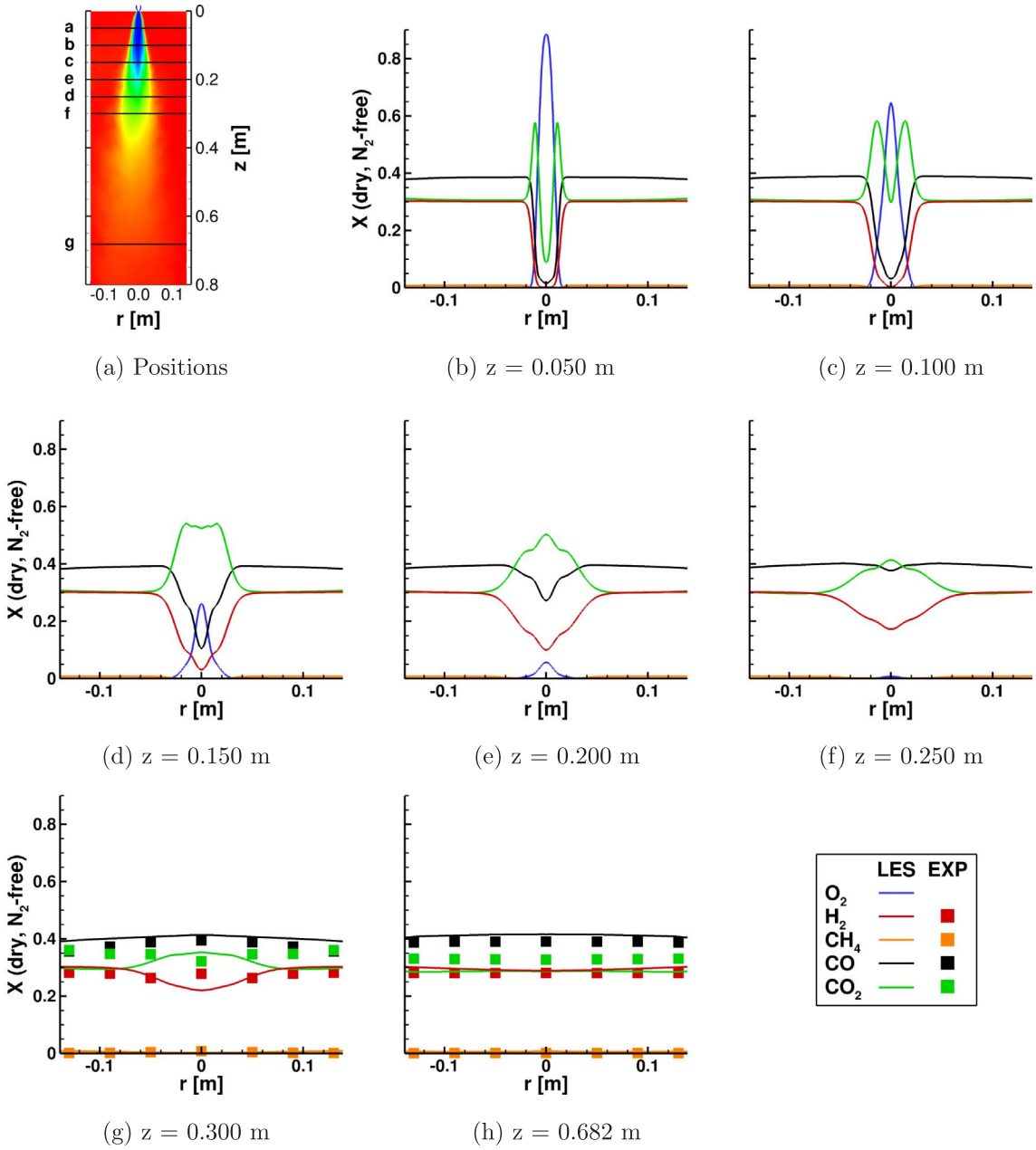

Fig. 14. Time- and angular-averaged radial species mole fraction distributions (b)–(h) at the downstream positions depicted in (a): LES (lines) and experimental data (squares).

Acknowledgments

The research leading to these results has received funding from the Helmholtz Virtual Institute for Gasification Technology, HVIGasTech [45].

References

[1] Fleck S, Santo U, Hotz C, Jakobs T, Eckel G, Mancini M, Weber R, Kolb T. Entrained flow gasification. Part 1: Gasification of glycol in an atmospheric-pressure experimental rig. Fuel 2018;217:306–19.
[2] Mancini M, Alberti M, Dammann M, Santo U, Eckel G, Kolb T et al. Entrained flow gasification. Part 2: Mathematical modeling of the gasifier using rans method, Fuel.
[3] Warnatz J, Maas U, Dibble R. Combustion – physical and chemical fundamentals, modeling and simulation, experiments, pollutant formation. 4th Edition Berlin Heidelberg: Springer; 2006.
[4] Gräbner M. Gasification of solids: past, present, and future. Wiley-VCH Verlag GmbH & Co. KGaA; 2014. Ch. 2, pp. 29–42.
[5] Pedel J, Thornock JN, Smith PJ. Large eddy simulation of pulverized coal jet flame ignition using the direct quadrature method of moments. Energy Fuels 2012;26(11):6686–94.
[6] Franchetti B, Marincola FC, Navarro-Martinez S, Kempf A. Large eddy simulation of a pulverised coal jet flame. Proc Combust Inst 2013;34(2):2419–26.
[7] Stein O, Olenik G, Kronenburg A, Cavallo Marincola F, Franchetti B, Kempf A, Ghiani M, Vascellari M, Hasse C. Towards comprehensive coal combustion modelling for LES. Flow Turbulence Combust 2013;90(4):859–84.
[8] Olenik G, Stein O, Kronenburg A. Les of swirl-stabilised pulverised coal combustion in {IFRF} furnace no. 1. Proc Combust Inst 2015;35(3):2819–28.
[9] Rabaçal M, Franchetti B, Marincola FC, Proch F, Costa M, Hasse C, Kempf A. Large eddy simulation of coal combustion in a large-scale laboratory furnace. Proc Combust Inst 2015;35(3):3609–17.
[10] Boileau M, Pascaud S, Riber E, Cuenot B, Gicquel LYM, Poinsot TJ, Cazalens M. Investigation of two-fluid methods for large eddy simulation of spray combustion in gas turbines. Flow Turbulence Combust 2008;80(3):291–321.
[11] Patel N, Menon S. Simulation of spray-turbulence-flame interactions in a lean direct injection combustor. Combust Flame 2008;153(1-2):228–57.
[12] Chrigui M, Gounder J, Sadiki A, Masri AR, Janicka J. Partially premixed reacting acetone spray using {LES} and {FGM} tabulated chemistry. Combust Flame 2012;159(8):2718–41 Special Issue on Turbulent Combustion.
[13] Ukai S, Kronenburg A, Stein O. LES-CMC of a dilute acetone spray flame. Proc Combust Inst 2013;34(1):1643–50.
[14] Sacomano Filho FL, Chrigui M, Sadiki A, Janicka J. LES-based numerical analysis of droplet vaporization process in lean partially premixed turbulent spray flames. Combust Sci Technol 2014;186(4–5):435–52.

[15] Heye C, Raman V, Masri AR. Influence of spray/combustion interactions on auto-ignition of methanol spray flames. Proc Combust Inst 2015;35(2):1639–48.
[16] Jones W, Marquis A, Vogiatzaki K. Large-eddy simulation of spray combustion in a gas turbine combustor. Combust Flame 2014;161(1):222–39.
[17] Jones W, Marquis A, Noh D. LES of a methanol spray flame with a stochastic sub-grid model. Proc Combust Inst 2015;35(2):1685–91.
[18] Ghani A, Poinsot T, Gicquel L, Müller J-D. LES study of transverse acoustic instabilities in a swirled kerosene/air combustion chamber. Flow Turbulence Combust 2016;96(1):207–26.
[19] Abani N, Ghoniem AF. Large eddy simulations of coal gasification in an entrained flow gasifier. Fuel 2013;104:664–80.
[20] Löwe J, Probst A, Knopp T, Kessler R. A low-dissipation low-dispersion second-order scheme for unstructured finite-volume flow solvers. In: 53rd AIAA Aerospace Sciences Meeting, Kissimmee, Florida; 2015.
[21] Sagaut P, Deck S, Terracol M. Multiscale and multiresolution approaches in turbulence. Imperial College Press; 2006.
[22] Pope S. Turbulent flows. Cambridge: Cambridge University Press; 2000.
[23] Fröhlich J. Large Eddy Simulation turbulenter Strömungen. B.G: Teubner Verlag/GWV Fachverlage GmbH; 2006.
[24] Poinsot T, Veynante D. Theoretical and numerical combustion. 3rd ed. Toulouse: CNRS; 2011.
[25] Gerlinger P. Numerische Verbrennungssimulation – Effiziente numerische Simulation turbulenter Verbrennung. Berlin: Springer; 2005.
[26] Noll B. Möglichkeiten und Grenzen der numerischen Beschreibung von Strömungen in hochbelasteten Brennräumen. Universität Karlsruhe; 1992.
[27] Ducros F, Nicoud F, Poinsot T. A wall-adapting local eddy-viscosity model for simulations in complex geometries. In: Conference on Numerical Methods for Fluid Dynamics, Oxford, UK; 1998.
[28] Nicoud F, Ducros F. Subgrid-scale stress modelling based on the square of the velocity gradient tensor. Flow Turbulence Combust 1999;62(3):183–200.
[29] Boussinesq J. Essai sur la théorie des eaux courantes. Rapport sur un mémoire de M. Boussinesq, Mémoires présentés par divers savants à l'Académie des sciences de l'Institut de France: sciences mathématiques et physiques 1 (1877) XXII–680.
[30] Probst A, Löwe J, Reu S, Knopp T, Kessler R. Scale-resolving simulations with a low-dissipation low-dispersion second-order scheme for unstructured finite-volume flow solvers. In: 53rd AIAA Aerospace Sciences Meeting, Kissimmee, Florida; 2015.
[31] Di Domenico M. Numerical simulations of soot formation in turbulent flows Ph.D. thesis Fakultät für Luft- und Raumfahrttechnik und Geodäsie, Universität Stuttgart; 2008.
[32] Ivanova E. Numerical simulations of turbulent mixing in complex flows Ph.D. thesis Institute of Combustion Technology for Aerospace Engineering, University of Stuttgart; 2012.
[33] Kuo KK. Principles of combustion. New York: Wiley; 1986.
[34] Hafner S. Modellentwicklung zur numerischen simulation eines flugstromvergasers für biomasse. Ruprechts-Karls-Universität Heidelberg; 2010. [Ph.D. thesis].
[35] Hafner S, Rashidi A, Baldea G, Riedel U. A detailed chemical kinetic model of high-temperature ethylene glycol gasification. Combust Theor Model 2011;15(4):517–35.
[36] Kathrotia T, Naumann C, Owald P, Köhler M, Riedel U. Kinetics of ethylene glycol: the first validated reaction scheme and first measurements of ignition delay times and speciation data. Combust Flame 2017;179:172–84.
[37] Abramzon B, Sirignano W. Droplet vaporization model for spray combustion calculations. Int J Heat Mass Transfer 1989;32(9):1605–18.
[38] Clift R, Grace JR, Weber ME. Bubbles, drops, and particles. New York: Academic Press; 1978.
[39] Bini M, Jones WP. Large-eddy simulation of particle-laden turbulent flows. J Fluid Mech 2008;614:207–52.
[40] Gardiner CW. Handbook of stochastic methods: for physics, chemistry and the natural sciences. 3rd ed. Berlin; Heidelberg [u.a.]: Springer; 2004.
[41] Leboissetier A, Okong'o N, Bellan J. Consistent large-eddy simulation of a temporal mixing layer laden with evaporating drops. Part 2. a posteriori modelling. J Fluid Mech 2005;523:37–78.
[42] Jakobs T, Djordjevic N, Fleck S, Mancini M, Weber R, Kolb T. Gasification of high viscous slurry R&D on atomization and numerical simulation. Appl Energy 2012;93:449–56.
[43] Tropea C. Optical particle characterization in flows. Annu Rev Fluid Mech 2011;43(1):399–426.
[44] Bustamante F, Enick RM, Cugini A, Killmeyer RP, Howard BH, Rothenberger KS, Ciocco MV, Morreale BD, Chattopadhyay S, Shi S. High-temperature kinetics of the homogeneous reverse water-gas shift reaction. AIChE J 2004;50(5):1028–41.
[45] Kolb T, Aigner M, Kneer R, Müller M, Weber R, Djordjevic N. Tackling the challenges in modelling entrained-flow gasification of low-grade feedstock. J Energy Inst 2016;89(4):485–503.